Chemical Engineering Research and Design 232 (2026) 239–250

Contents lists available at ScienceDirect

Chemical Engineering Research and Design

journal homepage: www.elsevier.com/locate/cherd

Fluid dynamic characterization and operating window analysis of a pilot-scale multiphase loop reactor for biotechnological applications

Diana Wall [a,*], Maurice Bastard [a], Andreas Jupke [a,b,*]

[a] Institute of Fluid Process Engineering, RWTH Aachen University, Forckenbeckstr. 51, 52074 Aachen, Germany
[b] Institute for Bio- and Geosciences (IBG-2), Forschungszentrum Jülich GmbH, 52428 Jülich, Germany

ARTICLE INFO

Keywords:
Multiphase loop reactor
in situ product removal
Bioreactor
Bioprocess intensification
Pilot plant
Gas holdup
Aqueous velocities
Volumetric mass transfer parameter
Mixing time

ABSTRACT

Bioprocess intensification through in situ product extraction can mitigate product inhibition and extend fermentation duration. However, conventional stirred-tank reactors often generate fine solvent dispersions and stable emulsions, which complicate subsequent phase separation. A multiphase loop reactor (MPLR), based on a modified airlift design with a concentric draft tube, offers a promising alternative by spatially separating aeration from organic-phase dispersion and thereby enabling simultaneous fermentation and liquid–liquid extraction. Building on previous laboratory-scale studies, this work establishes a pilot-scale facility dedicated to fluid-dynamic characterization without biocatalytic conversion, with the aim of providing a basis for a projected operational window for future three-phase operation. Key hydrodynamic parameters relevant to process design and operation were determined in two-phase experiments, including gas holdup, volumetric mass transfer coefficient, mixing time, and liquid circulation velocity. Steady state conditions are reached within 15 s, as identified by a constant gas holdup. Further, it was shown that sufficient oxygen transfer, corresponding to $k_La \geq 100\,h^{-1}$, is achieved at superficial gas velocities of $0.02\,m\,s^{-1}$ and above. At superficial gas velocities of $0.01\,m\,s^{-1}$ and above, mixing times below 30 s indicate that the reactor can be considered well-mixed. The liquid flow field was characterized from velocity distributions across the reactor cross-section, confirming the expected circulation between downcomer and riser. Based on the measured two-phase fluid dynamics, the potential feasibility of three-phase counter-current operation was assessed by relating the downward aqueous-phase velocity in the downcomer to droplet rise behavior. A critical droplet diameter was derived using the Schiller–Naumann correlation as a conservative estimate of droplet rise velocity. Additional three-phase experiments in the accessible low-aeration regime support the use of this approach as a conservative basis for preliminary design assessments. By combining this hydrodynamic constraint with the measured mass transfer and mixing characteristics, a first-order operating window for the MPLR was established. The resulting analysis provides a first-order estimate of operating conditions under which sufficient oxygen transfer and rapid mixing may coexist with model-predicted feasibility for counter-current extraction.

1. Introduction

Bioprocesses are increasingly recognized as sustainable alternatives to fossil-based production, enabling the manufacture of bio-based chemicals and fuels while supporting the transition toward a circular economy (Yusuf and Ojedokun, 2024; Adedeji Olalekan Iwogbemi, 2025). A major limitation in many bioprocesses is product inhibition, in which the accumulation of cytotoxic products reduces cell viability and metabolic activity. This leads to low titers and yields and therefore in low final product concentrations (Zhang et al., 2015; Kennedy et al., 2024; Park and Geng, 1992; Maiorella et al., 1983). Process intensification through *in situ* product removal (ISPR) offers a means to mitigate inhibition by maintaining product concentrations below toxic thresholds (Maiorella et al., 1983; Lee et al., 2019; Salas-Villalobos et al., 2021). Various ISPR strategies have been developed to tackle this challenge. These include liquid–liquid extraction, crystallization, adsorption, membrane-based separations such as pervaporation and membrane extraction, foam fractionation, and gas stripping (Salas-Villalobos et al., 2021; Park and Geng, 1992; Xue et al., 2015; Weilnhammer and Blass, 1994). Among these, liquid–liquid extraction is particularly suitable for hydrophobic or moderately polar products due to favorable distribution coefficients (Weilnhammer and Blass, 1994). In this approach, an additional immiscible organic

* Corresponding authors.
E-mail addresses: diana.wall@avt.rwth-aachen.de (D. Wall), andreas.jupke@avt.rwth-aachen.de (A. Jupke).

https://doi.org/10.1016/j.cherd.2026.06.054
Received 17 March 2026; Received in revised form 24 June 2026; Accepted 26 June 2026
Available online 3 July 2026
0263-8762/© 2026 The Authors. Published by Elsevier Ltd on behalf of Institution of Chemical Engineers. This is an open access article under the CC BY license (http://creativecommons.org/licenses/by/4.0/).

liquid phase is introduced alongside the aqueous fermentation broth. The target product distributes between the phases, thereby reducing the concentration in the aqueous phase and alleviating inhibitory effects (Chaichol and Weeranoppanant, 2023; De Brabander et al., 2021).

By adding the organic phase in conventional stirred-tank fermentations, however, the high impeller speeds required to ensure adequate oxygen transfer often generate fine solvent dispersions. Various biochemical molecules in the fermentation broth, which behave like surfactants, increase the stability of the resulting emulsion. These emulsions complicate subsequent phase separation and product recovery, making downstream processing more demanding (Chaichol and Weeranoppanant, 2023). Various methods are being developed to deal with emulsions (Alicke et al., 2025). One promising approach focuses on avoiding emulsification by employing larger solvent droplets (Fontenot and Schork, 1993; Dianingsih et al., 2016). Based on this concept, a promising reactor design is the multiphase loop reactor (MPLR), which utilizes larger solvent droplets to suppress emulsification. The MPLR is a modified airlift reactor design equipped with a concentric draft tube that is intended for simultaneous fermentation and extraction within a single vessel (Bednarz et al., 2017). The reactor consists of two main zones: a riser for gas introduction, and a downcomer for the introduction of the organic phase, enabling counter-current *in situ* extraction. The introduced air induces a density difference between the riser and the downcomer. This creates an internal circulation of the continuous aqueous phase, in which the fermentation broth rises in the riser and descends in the downcomer. By introducing an organic phase with a lower density than the aqueous medium, it ascends through the downcomer due to the density difference, establishing counter-current extraction. At the top of the reactor, a coalescer facilitates phase separation, allowing the organic phase enriched with the extracted product to be withdrawn (Bednarz et al., 2017).

This reactor concept has previously been demonstrated at a 5 L laboratory scale for the production of rhamnolipids using Pseudomonas putida (von Campenhausen et al., 2023) and methyl ketones using Pseudomonas taiwanensis VLB120 (Grütering et al., 2024). These proof-of-concept studies confirm the technical feasibility of coupling microbial production with extraction in a single integrated system and provide a basis for further scale-up investigations.

To progress from lab-scale validation, it is essential to characterize the reactor's fluid dynamics and identify conditions that ensure stable and efficient operation. As fermentation and extraction occur simultaneously within a single vessel, operating conditions must be compatible with both biological and hydrodynamic requirements. Establishing this operational window therefore requires identification and quantitative characterization of the fluid dynamic parameters and phenomena that determine (i) formation of a stable internal water circulation, (ii) avoidance of solvent flooding into the riser, (iii) adequate oxygen supply, and (iv) homogeneous mixing to sustain microbial activity (Li et al., 2022). In order to determine these operating conditions, key fluid dynamic parameters require quantification. These include the gas holdup in the riser, the relative velocity between the organic and aqueous phases in the downcomer, the oxygen transfer coefficient, and the mixing time. The gas holdup ε_g is crucial as it directly affects the stability of the internal circulation within the reactor, which is essential for maintaining continuous phase interactions. It is generally defined as the volumetric fraction of gas in the complete volume of all phases V_{all} (Hwang and Cheng, 1997). In order to establish counter-current extraction in the outer compartment of the reactor, it is necessary that the rising organic phase in the downcomer is not carried away by the water phase into the riser. The conditions for this can be estimated based on the condition that the aqueous velocity in the downcomer is lower than that of the rising organic droplets. By determining this velocity, it is possible to estimate in advance the minimum size of droplets of a particular organic compound at which counter-current extraction in the reactor is feasible.

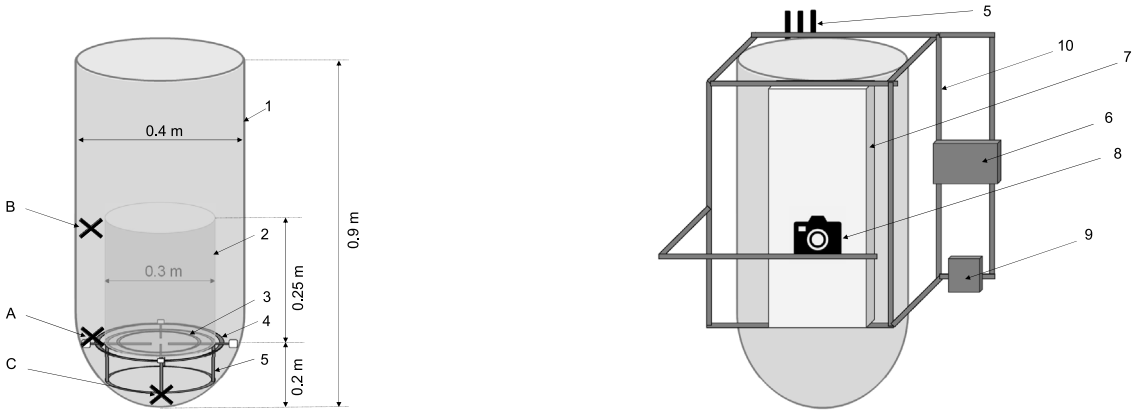
The oxygen transfer coefficient $k_L a$ is used to quantify the rate at which oxygen is transferred from the gas phase to the continuous aqueous phase. It provides a direct measure of the oxygen availability for the microorganisms, which in turn influences their metabolic activity and productivity. Efficient gas–liquid transfer ensures that the aqueous phase remains adequately oxygenated throughout the reactor and can be determined based on the oxygen mass balance (Garcia-Ochoa and Gomez, 2009). Furthermore, it is necessary that similar conditions prevail throughout the reactor. Excessive local differences in pH-values, substrate concentrations or temperatures have a significant impact on the performance of the microorganisms (Doran, 1995). The mixing time t_{mixing} can be used to quantify the mixing and homogeneity that is relevant for nutrient supply, control strategies and biological stability (Christi and Moo-Young, 1987).

Hydrodynamic investigations at laboratory scale are commonly constrained by pronounced wall effects resulting from small reactor diameters and added probes (Kalaga et al., 2017). These effects distort local flow fields and bias measurements of hydrodynamic parameters, limiting their transferability to larger scales (Bai, 2010). The multiphase loop reactor can be conceptually divided into a riser, which behaves like a bubble column (Li et al., 2022), and a downcomer, which resembles an extraction column. The literature reports minimum diameters of approximately 0.15 m for bubble columns, above which wall effects and integrated sensor technology play only a minor role (Wilkinson et al., 1992). Similar considerations apply to extraction columns, where diameters of 0.05 m and above have been shown to have little impact on the column's overall performance (Smith et al., 2008).

Motivated by these limitations, a pilot-scale multiphase loop reactor was implemented to investigate the flow behavior of the reactor concept under scale-up-relevant operating conditions. In addition, a set of measurement methods was developed to characterize the target parameters within the pilot plant. The present study is experimentally limited to two-phase gas–liquid hydrodynamics using an air–water model system. Based on these measurements, theoretical considerations were subsequently employed to project the operating limits of the intended three-phase system. The applicability of the underlying model was partially assessed under three-phase conditions. The selected parameters thus provide a basis for a first-order estimation of relevant hydrodynamic constraints derived from the air–water system. While this approach does not capture the additional interfacial and rheological effects introduced by an organic solvent, it nevertheless facilitates a conservative initial assessment of the operating window under scale-relevant conditions.

2. Pilot plant and methods

The pilot plant consists of a vessel with internals, mounted in an Item profile frame. Additionally, the frame accommodates the measurement instrumentation and control systems. The cylindrical glass vessel with a hemispherical bottom has a total volume of up to 100 L, a diameter of 0.4 m, and a total height of 0.9 m. The hemispherical bottom itself has a depth of 0.2 m. Inside the vessel, a support foot is installed, providing a base for positioning the draft tube and the sparger. The reactor configuration, including the internal structures and detailed dimensions, is shown in Fig. 1(a). Aeration is provided via the in-house compressed air line. The gas volume flow is adjusted using a Bronkhorst mass flow controller and can be adjusted between 4 and 175 L min^{-1}. The Item profile frame allows the installation of radial support rods, which are used to stabilize and fix the draft tube within the reactor. The same mounting system is employed to flexibly position measurement probes at arbitrary radial and axial locations inside the vessel. Three oxygen probes are installed and connected via a transmitter to the data acquisition system. For optical measurements, two viewing windows are located at the front and rear of the vessel. These windows can be filled with water to correct for light refraction. Uniform back-lighting is provided by an LED panel positioned at the rear of the reactor, while



(a) Overview of the multiphase loop reactor. (b) Overview of the pilot plant.

Fig. 1. Overview over the pilot plant of the multiphase loop reactor: 1: Glass vessel 2: Draft tube 3: Sparger 4: Organic disperser 5: Support foot A: $k_L a$ Position lower draft tube DC B: $k_L a$ Position upper draft tube DC C: $k_L a$ Position bottom 5: Optical oxygen probes 6: Transmitter 7: Correction window 8: Camera 9: Mass Flow controller 10: Item frame.

a front-mounted support enables the installation of imaging devices, including an industrial camera MER2-160-227U3C from GetCameras and a Sony Alpha 6000, for image acquisition. The draft tube used in this work has a height of 0.25 m, an outer diameter of 0.3 m and a wall thickness of 4 mm. The relatively low aspect ratio was selected to ensure strong internal circulation in a controlled pilot-scale environment. The support foot is designed such that the entire hemispherical bottom is represented within the bottom region of the reactor. The sparger employed in this study is a ring aerator with a diameter of 0.25 m, featuring 18 evenly distributed orifices with a diameter of 0.5 mm. The organic phase was introduced through a ring distributor with a diameter of 0.35 m, equipped with 18 evenly distributed orifices of the same diameter of 0.5 mm. Organic phase circulation was established using an ISMATEC gear pump to supply the organic phase and a Shenchen peristaltic pump for its withdrawal. The volumetric flow rate was monitored by an Bopp & Reuther Messtechnik oval gear flow meter installed in the feed line. To illustrate the overall process configuration, a schematic of the pilot plant is provided in Fig. 1(b).

2.1. Volume-expansion method

The gas holdup $\epsilon_{g,Riser}$ was determined using the volume-expansion method (Luo and Al-Dahhan, 2010; Zhong et al., 2022), applied exclusively to the riser section. Prior to aeration, the unaerated liquid height H_0 was determined after subtracting the hemispherical bottom volume V_{bottom} from the total liquid volume $V_{filling}$ to ensure that only the cylindrical riser section A_{Riser} was considered. Aeration was then initiated at the target gas volume stream $\dot{V}_g$. Image-based analysis in MatLab is performed on recordings restricted to the riser field of view. Each frame is globally binarized and complemented in inverse colors to enhance phase contrast. To eliminate noise and small artifacts, for example water droplets adhering to the vessel wall, the binary images are processed using the filter `bwareaopen` with a threshold of 150 pixels. The resulting binary mask is subdivided into vertical strips of 15 pixels width, and local gas–liquid interface positions were determined within each strip by adaptive binarization. The median interface height H_g across all strips was taken as the representative liquid level for that frame. Subsequently, the mean value and standard deviation of the heights are determined for all frames of the trial video. Using a prior geometric calibration, the pixel-based height was converted to metric values. This enables the determination of $\epsilon_{g,Riser}$ using the formula:

$$\epsilon_{g,Riser} = \frac{(H_g - H_0) \cdot A_{Riser}}{(H_g - H_0) \cdot A_{Riser} + V_{filling} - V_{bottom}}. \quad (1)$$

Preliminary experiments indicated that, once steady state is reached, extending video recordings beyond three seconds does not improve the determination of the gas holdup. Additionally to the investigations of the hold up at steady state conditions for various superficial gas velocities, the complete start-up sequences were recorded to determine the time required for the flow to stabilize, with the recording duration extended to three minutes.

2.2. Dynamic gassing-out method

The volumetric oxygen transfer coefficient $k_L a$ was determined via the dynamic gassing-out method (Garcia-Ochoa and Gomez, 2009). The liquid phase was first deoxygenated below 20 % air saturation $C_{O_2,0}$ by sparging nitrogen. Aeration was then switched to compressed air at the target gas volume flow rate, and the resulting increase in dissolved oxygen concentration C_{O_2} was recorded over the time until it reached the saturation oxygen concentration $C^*_{O_2}$. The obtained $k_L a$ values represent apparent volumetric mass transfer coefficients under non-ideal hydrodynamic conditions, as the dynamic response inherently includes both diffusive and convective contributions to oxygen transport. Since these apparent values are specific to the investigated reactor and its hydrodynamic conditions, they are hereafter referred to simply as $k_L a$. As such, the measured values should be interpreted as an effective measure of local oxygen transfer capacity rather than a purely intrinsic mass transfer coefficient. The volumetric oxygen transfer coefficient could be determined from the logarithmic slope of the oxygen concentration-time profile out of formula (2).

$$\ln\left(\frac{C^*_{O_2} - C_{O_2}}{C^*_{O_2} - C_{O_2,0}}\right) = -k_L a \cdot t. \quad (2)$$

The dissolved oxygen was measured using optical oxygen probes FDO® 925 from Xylem Analytics installed in vertically adjustable diving tubes, which were sealed at the bottom to ensure water-tightness. The probes were installed radially using the tank support system. To prevent bubble adhesion and measurement interference, protective metal mesh cages were attached under the probe heads to shield the sensors from direct contact with bubbles. The measurement data was retrieved from the data acquisition system KM 3000 from Xylem Analytics and synchronized with the system clock of the measurement computer, as the transmitter does not provide time-stamped signals with second-level resolution. The measurements were taken at several positions within the reactor to detect spatial variations in $k_L a$. In this study, the probes

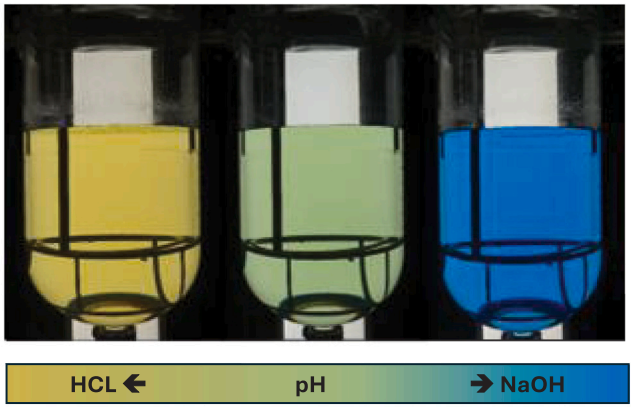


Fig. 2. Multiphase loop reactor containing bromothymol blue as a pH indicator, showing yellow coloration in the acidic range, green at neutral pH, and blue in the basic range. (For interpretation of the references to color in this figure legend, the reader is referred to the web version of this article.)

were positioned at three locations within the reactor: at the upper end of the draft tube in the downcomer, at the lower end of the draft tube in the downcomer, and in the bottom region of the reactor. Each of the three probes was successively measured at each position to exclude probe-specific effects.

2.3. Mixing time determination

Mixing time t_{mixing} in the reactor was determined using bromothymol blue as a pH-sensitive tracer. The indicator solution was prepared according to the supplier's instructions and diluted 500-fold, resulting in a color spectrum from yellow under acidic conditions, through green at neutral pH, to blue under basic conditions, as shown in Fig. 2. Initially, 0.5 mL of 1 mol L^{-1} NaOH was added to obtain a fully blue color state. Mixing was initiated by the addition of 1 mL of 1 mol L^{-1} HCl, followed by back-mixing via the addition of 1 mL of 1 mol L^{-1} NaOH. The reactor was illuminated using an LED panel, and the entire mixing process was recorded using a Sony Alpha 6000 camera positioned 0.5 m from the reactor. The applied optical tracer-based approach provides a global measure of mixing time and is therefore suitable for capturing reactor-scale mixing dynamics in multiphase systems. The red channel of the recorded RGB signal was evaluated as a function of time, as it showed the highest sensitivity to the color transition and the best agreement with manually evaluated mixing times. The mixing time was defined as the time required for the red value to increase at the mixing experiments from 5 % to 99 % and to decrease at the back-mixing trials from 95 % to 1 %. In addition to the investigated gas volumetric flow rates on the mixing time, it was determined under conditions of pure diffusion when the reactor was not aerated. Preliminary experiments were conducted to assess whether the addition of acid and base affects the fluid properties and, consequently, the hydrodynamics. For this purpose, up to 100 mmol NaH_2PO_4 and Na_2SO_4 were added to the reactor as a salt and the holdup was measured. No change in holdup was observed for additions up to 50 mmol. Therefore, the maximum number of acid or base additions of 1 mol L^{-1} was set at 50. After reaching this limit, the reactor content is completely replaced for further experiments. While salt addition tests confirmed no significant change in gas holdup, potential effects of pH indicators on surface tension and bubble coalescence were not directly quantified. However, the consistent mixing time trends across multiple gas velocities suggest that the method is robust for comparative characterization.

2.4. Particle tracking velocimetry

The velocity of the aqueous phase v_{aq} was determined using particle tracking velocimetry (PTV) with alginate beads as tracer particles. The tracer trajectories were corrected for gravitational settling and, subsequently, an acceleration-based correction was applied to compensate for particle–fluid inertial lag (Maxey and Riley, 1983). Alginate beads were prepared in-house using a alginate and calcium chloride solution and were designed to be neutrally buoyant with a density equal to that of the aqueous phase $\rho_p = 998\,kg\,m^{-3}$ with a nominal diameter of d_p = 3 mm. To quantify the quiescent settling contribution, tracer particles were recorded at zero imposed liquid flow rate, yielding the settling velocity $v_{p,0}$ (Clift et al., 1978). For each operating point, high-speed videos of 5 s duration were recorded at 220 frames per second. A trained PTV network was used to identify particles and organic droplets, assign unique identifiers to them, and track them across consecutive frames. The spatial pixel-to-length conversion calibration was obtained from the known field-of-view height and focus-based calibration, enabling position measurements on an x–y grid and thus velocity extraction from frame-to-frame displacement. Measurements were performed at multiple spatial locations within the reactor at the same axial height to determine the velocity distribution across the reactor cross-section. The particles were recorded in a horizontal cross-sectional plane located 0.120 m above the bottom of the draft tube. For the readial position r = 0.080 m – 0.185 m, the camera field of view covered an axial range from 0.085 m to 0.155 m above the draft-tube bottom, whereas at the radial position r = 0.0 m it ranged from 0.075 m to 0.165 m. This difference is attributed to the camera viewing angle and the adjusted focus setting for the central measurement positions, resulting in an increased axial field of view.

Let v_p denote the measured particle velocity component along the main flow direction. In the downcomer, the corrected particle velocity was computed as

$$v_{p,corr}^{DC} = v_p - v_{p,0}, \tag{3}$$

where the particle velocity was corrected to remove the influence of gravitational forces. In the riser, the particle velocity was corrected not only for gravitational effects but also for the impact of the gas phase on the velocity using the measured hold up in the riser section $\varepsilon_{g,Riser}$ via

$$v_{p,corr}^{R} = (v_p + v_{p,0}) \cdot (1 - \varepsilon_{g,Riser}) \tag{4}$$

In addition to mean velocities, particle accelerations were computed from tracked trajectories using particles that were visible for at least five consecutive frames. For each trajectory, the particle acceleration a_p was used to infer the instantaneous particle-fluid slip speed s by solving a nonlinear drag balance (Brennen, 2005). The projected cross-sectional area of the particle A_p and volume V_p were computed as

$$A_p = \frac{\pi d_p^2}{4}, \tag{5}$$

$$V_p = \frac{\pi d_p^3}{6}. \tag{6}$$

With the fluid density of the continuous phase ρ_c, particle density ρ_p, and dynamic viscosity μ, the effective particle mass m_{eff}, incorporating the added mass term for a sphere (Maxey and Riley, 1983; Clift et al., 1978), was defined as

$$m_{eff} = V_p \left(\rho_p + 0.5\,\rho_c\right). \tag{7}$$

The Reynolds number Re was expressed in terms of the slip speed s as

$$Re = \frac{\rho_c d_p s}{\mu}. \tag{8}$$

The drag coefficient C_d was evaluated using the standard Schiller–Naumann correlation (Schiller and Naumann, 1933):

$$C_d = \begin{cases} \frac{24}{Re}\left(1 + 0.15\, Re^{0.687}\right), & Re \le 1000, \\ 0.44, & Re > 1000, \end{cases} \tag{9}$$

and the drag force was written as

$$F_d = \frac{1}{2}\,\rho_c\, C_d\, A_p\, s^2. \tag{10}$$

Assuming that the measured particle acceleration magnitude $|a_p|$ is generated by the drag response (Clift et al., 1978), the slip speed s was obtained from

$$\frac{1}{2}\,\rho_c\, C_d\, A_p\, s^2 = m_{eff}\,|a_p|. \tag{11}$$

The aqueous-phase velocity was reconstructed from the measured particle velocity and the inferred slip contribution as (Maxey and Riley, 1983; Clift et al., 1978)

$$v_{aq} = v_{p,corr} + \mathrm{sign}(a_p)\, s, \tag{12}$$

where the $\mathrm{sign}(\cdot)$ preserves the direction of the acceleration. This approach is applicable under the assumption of rigid, spherical particles with constant shape, negligible wall effects, and dilute conditions. In the present study, the particles remain rigid and spherical in the medium, no wall-induced effects were observed, and the particle volume fraction was approximately 0.2 vol.%, such that particle–particle interactions can be neglected (Zaidi, 2020). The PTV method was also applied to measure the diameter and velocity of organic droplets. Droplet measurements were conducted in a horizontal cross-sectional plane located 0.120 m above the bottom of the draft tube at a radial position of $r = 0.175$ m, corresponding to the center of the downcomer. For evaluation of droplet size distribution and corresponding velocities, the detected droplets were classified into discrete diameter bins with a bin width of 0.1 mm.

2.5. Experiment procedure

For all experiments, the same reactor geometry and a fill level of 60 L were used. The gas volumetric flow rates were varied between 4, 40, 80 and 175 L min^{-1}, corresponding to superficial gas velocities u_g of 10×10^{-4}, 10×10^{-3}, 2×10^{-2} and 4.4×10^{-2} m s^{-1}, respectively. Experiments were conducted at room temperature, as the established methods are not sensitive to small variations in temperature. The organic phase experiments were performed using 2-undecanone as the organic solvent, operating at pumping rates of 0.26 L min^{-1} and 0.54 L min^{-1}. Each measurement was repeated three times to ensure reproducibility, and the mean and standard deviation of these measurements were subsequently calculated. Specific parameter settings for each method are detailed in the respective method sections.

3. Results and discussion

This section presents the results for the target parameters obtained in the pilot plant using the setup described above. All results presented in the first sections are based on gas–liquid operation. In the final subsection, the potential extension to gas–liquid-organic operation is considered. The discussion is based on theoretical considerations and is complemented by initial three-phase experiments to assess the underlying assumptions. The combined findings are then used to derive a preliminary operating window for three-phase operation.

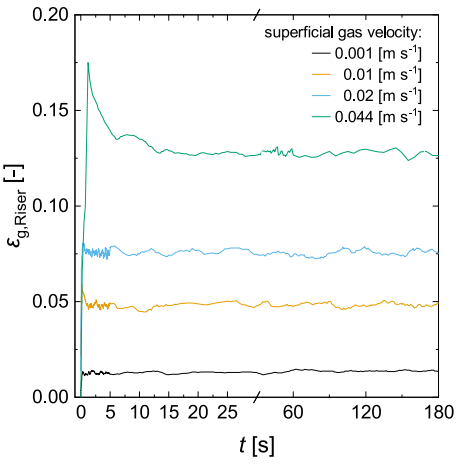
3.1. Holdup investigation in the multiphase loop reactor

Fig. 3(a) shows the transient response of the system to changes in superficial gas velocity for four different gas superficial velocities. At low to medium gas velocities, this stabilization to steady state occurs within less than 5 s, whereas at high velocities, as 0.044 m s^{-1}, 15 s are required to reach a stable value. Accordingly, steady state can be assumed after 15 s in the present reactor, and subsequent measurements of all target parameters are representative. Fig. 3(b) presents the gas holdup in the already stabilized state at various gas superficial velocities. The general trend shows that the holdup increases with increasing gas superficial velocity, which is consistent with physical expectations and the literature, as more gas is introduced into the system. Holdup measurements provide a sensitive indicator of the reactor's fluid dynamic behavior, as variations in the slope of the holdup can reveal changes in flow patterns or phase distribution within the system (Hwang and Cheng, 1997). In the present study, a change in slope is observed in the superficial gas velocity range of 0.001–0.01 m s^{-1}, suggesting a potential transition in flow regime within this range. These variations are primarily caused by bubble coalescence (Hwang and Cheng, 1997), and consequently, they also influence all other key fluid dynamic parameters in the reactor.

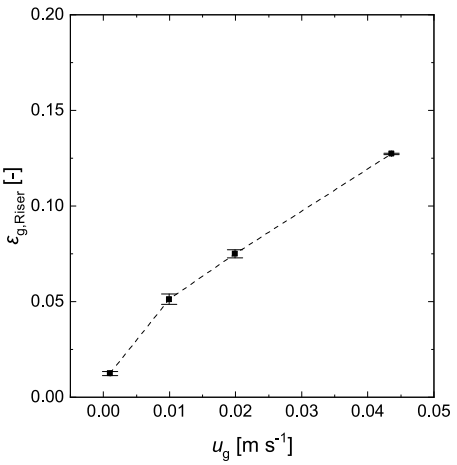
3.2. Oxygen availability in the multiphase loop reactor

The experimentally determined volumetric mass transfer coefficients k_La are shown in Fig. 4 as a function of the gas superficial velocity. The plot includes measurements at three different positions within the multiphase loop reactor: the downcomer at the height of the lower edge of the draft tube (Position A), the downcomer at the height of the upper edge of the draft tube (Position B), and the riser in the bottom region (Position C). Each measurement position was investigated using all three available dissolved oxygen probes in order to exclude a potential probe-specific influence on the measured k_La-values. Since the observed trends were reproducible regardless of the probe used, a systematic sensor-induced bias can be ruled out. The applied dynamic gassing-out method is used for the comparative analysis of spatially resolved k_La-values under different hydrodynamic conditions. Across all measurement positions, a clear increase in k_La with increasing gas superficial velocity is observed. This trend is in good agreement with literature reports, which describe an enhanced gas–liquid mass transfer performance at higher gas superficial velocities due to improved hydrodynamics and increased gas dispersion (Garcia-Ochoa and Gomez, 2009). At low gas superficial velocities, the local k_La-values at the three positions differ only marginally, supporting the commonly stated assumption of good overall mixing in airlift reactors (Christi and Moo-Young, 1987), where the exact probe location has only a minor influence on the measured k_La. At higher gas superficial velocities, however, distinct position-dependent differences become apparent. In particular, the downcomer at the height of the lower draft tube edge consistently exhibits the lowest k_La-values. At the highest investigated gas superficial velocity, the k_La at this position is nearly 20 h^{-1} lower than the values measured in the riser bottom region and nearly 40 h^{-1} lower in the downcomer at the upper draft tube edge. The same qualitative behavior is already evident at a gas superficial velocity of 0.02 m s^{-1}, indicating a systematic limitation of gas–liquid mass transfer at the lower downcomer area.

While airlift reactors are often described as well-mixed on a global scale, the present results demonstrate that local mass transfer conditions can still vary significantly depending on the reactor zone and operating conditions. The observed spatial differences can be explained by considering the definition of the volumetric mass transfer coefficient, which is the product of the liquid-side mass transfer coefficient k_L and the specific interfacial area a. In the downcomer at the upper edge of the draft tube, a substantial fraction of gas bubbles is still present, resulting in a comparatively high specific interfacial area and thus enhanced gas–liquid mass transfer. In contrast, at the downcomer



(a) Determination of steady-state operation based on the time-resolved measurement of gas holdup after initiation of gas flow.



(b) Steady-state gas holdup in the riser at different superficial gas velocities.

Fig. 3. Overview of gas holdup investigations.

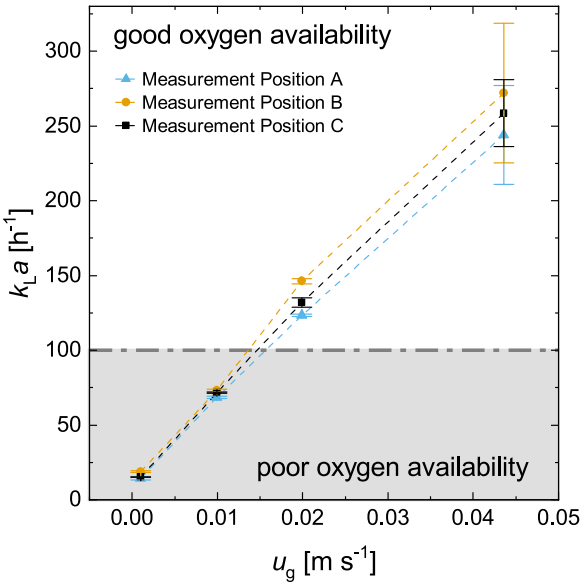


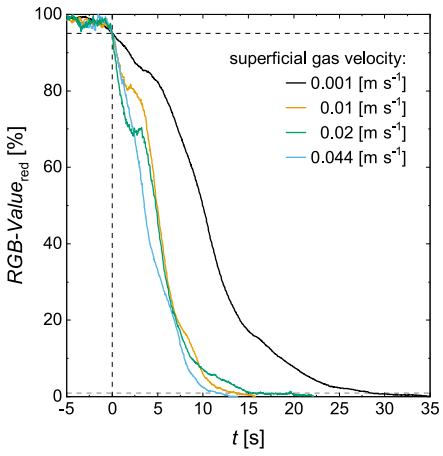
Fig. 4. Impact of position of probes on the gas–liquid mass transfer.

inlet near the lower edge of the draft tube, only very few gas bubbles are transported. The flow in this region is predominantly directed and characterized by low turbulence intensity, leading to minimal direct gas–liquid interaction. Consequently, the specific interfacial area a approaches very low values, which explains the significantly reduced local k_La. In the bottom region, local turbulence and the proximity to the gas sparging zone promote bubble dispersion into deeper reactor regions, thereby enhancing gas–liquid contact. With increasing gas superficial velocity, turbulence intensity in this region further increases, which contributes to an additional improvement of the local k_La.

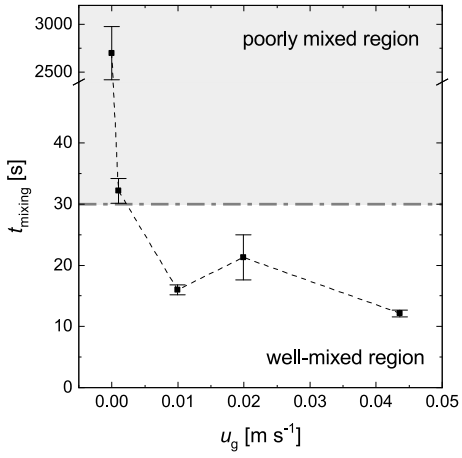
In summary, despite the generally good mixing performance of the airlift reactor, the local gas–liquid mass transfer is clearly position-dependent. The lowest mass transfer rates are consistently observed at the lower edge of the draft tube in the downcomer. This location therefore represents the most critical zone with respect to oxygen availability. Chisti et al. report that aerobic bacterial processes require oxygen transfer rates which, in airlift reactors with standard internal-loop geometries operated at industrially relevant aeration rates, typically correspond to volumetric mass transfer coefficients k_La of $100\,h^{-1}$ or above, depending on reactor geometry and operating conditions (Christi and Moo-Young, 1987). For highly active bacterial cultures such as *Pseudomonas* spp., which was used in the laboratory-scale proof-of-concept studies (von Campenhausen et al., 2023; Grütering et al., 2024), oxygen transfer becomes limiting under lower k_La-conditions due to the high cellular oxygen demand (Garcia-Ochoa and Gomez, 2009; Escobar et al., 2016; Demling et al., 2021). In the present study, a reference value of $k_La = 100\,h^{-1}$ (see Fig. 4) is therefore adopted as a conservative lower bound based on literature-reported oxygen uptake rates (Demling et al., 2021). This value is exceeded at superficial gas velocities of $0.02\,m\,s^{-1}$ and above in the investigated reactor configuration. Operation under these conditions can thus be considered suitable for aerobic biotechnological applications, with the downcomer inlet at the lower draft tube edge constituting the limiting region for oxygen transfer.

3.3. Mixing in the multiphase loop reactor

The results of the mixing experiments are shown in Fig. 5(a), where the temporal evolution of the normalized red color fraction of the RGB value within the reactor is plotted for four individual experiments corresponding to different gas superficial velocities. The red color fraction serves as an indicator for the temporal progression of mixing within the reactor vessel. Upon addition of NaOH, the color of the liquid inside the reactor changes from yellow to green and finally to blue. Accordingly, the red color fraction extracted from the frames decreases with time. The temporal evolution of this decrease differs depending on the applied gas superficial velocity. A comparison of the curves shows that, at low gas superficial velocities, the decay of the red color fraction proceeds more slowly than at higher gas superficial velocities. At the same time, the results demonstrate that an increase in gas superficial velocity does not necessarily lead to a proportional reduction in mixing time. Instead, individual experiments exhibit comparable or even longer mixing times despite higher gas superficial velocities. The mixing time is defined as the time at which only 1 % of the initial red color fraction remains detectable in the image. Based on this definition, mixing times can be unambiguously determined for all investigated operating conditions. A detailed comparison of individual experiments further illustrates this behavior. At



(a) Tracking of the red RGB-value during the mixing process of individual back-mixing experiments.



(b) Impact of the gas superficial velocity on the overall mixing time.

Fig. 5. Mixing experiments in the multiphase loop reactor. (For interpretation of the references to color in this figure legend, the reader is referred to the web version of this article.)

the beginning of the experiment, the curves corresponding to 0.01 m s^{-1}, 0.02 m s^{-1}, and 0.044 m s^{-1} show a similar initial trend characterized by a rapid decrease in the red color fraction. While the red fraction initially decreases more rapidly at 0.02 m s^{-1}, this trend is overtaken by the curve at 0.01 m s^{-1} after approximately 5 s. As a result, the overall mixing time at 0.02 m s^{-1} is longer than at 0.01 m s^{-1}. This effect is particularly pronounced in the bottom region of the reactor. At higher gas superficial velocities, intensified local turbulence leads to the formation of inhomogeneous mixing zones, causing certain regions to respond more slowly. Consequently, the time required for the entire reactor bottom to lose its red color fraction and reach a homogeneous blue coloration is increased. As shown in Fig. 5(b), where the mixing time is plotted against the superficial gas velocity, the mixing times at 0.01 to 0.044 m s^{-1} are at a similar level. The resulting mixing times are approximately 16 s at 0.01 m s^{-1} and around 20 s at 0.02 m s^{-1}. The shortest mixing time is observed at 0.044 m s^{-1}, with a value of roughly 12 s. In contrast, the longest mixing time under aerated conditions occurs at the lowest investigated superficial gas velocity of 0.001 m s^{-1} and exceeds 30 s. Much longer mixing times, on the order of three-quarters of an hour, are observed in the complete absence of aeration. In this case, no convective transport occurs, and mass transfer is purely driven by diffusion. Overall, the reactor exhibits rapid mixing over a broad range of gas superficial velocities, while significantly prolonged mixing times are observed only at very low gas superficial velocities. The non-monotonic trend is attributed to competing effects of increased turbulence and large-scale vortex formation, which can transiently reduce effective mixing efficiency.

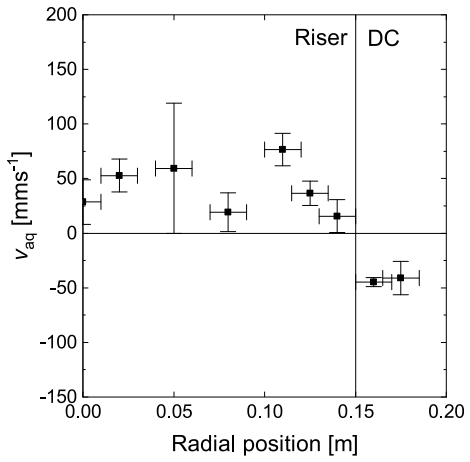
For biotechnological processes, a short mixing time is crucial in order to avoid pH gradients, nutrient inhomogeneities and local inhibition zones (Doran, 1995). According to Rosso, rapid mixing occurs in less than 30 s, ensuring thorough blending of chemicals into the liquor (Rosso et al., 2023). The mixing times determined in the range of approximately 12–18 s at medium to high gas superficial velocities are significantly below the critical value and can therefore be considered sufficiently short for biotechnological applications. Only at very low gas superficial velocities do significantly longer mixing times of over 30 s occur, which can potentially lead to inhomogeneous reactor conditions.

3.4. Aqueous velocity profile in the multiphase loop reactor

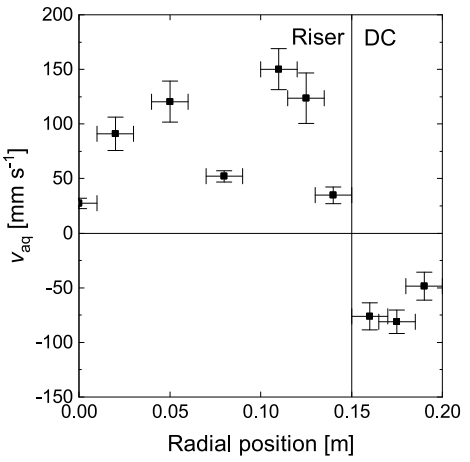
Particle tracking velocimetry measurements were performed to characterize the water phase flow in the modified air-lift reactor. This method allows for the determination of local aqueous-phase velocities across the reactor cross-section, providing critical information for the design and operation of future three-phase processes. The measured velocities were plotted over the reactor cross-section for different gas superficial gas velocities as shown in the diagrams in Fig. 6. Negative velocities are observed in the downcomer, while positive velocities occur in the riser, consistent with the expected overall liquid circulation pattern (Christi and Moo-Young, 1987). In the downcomer, velocities are relatively uniform, whereas in the riser the profile is highly non-uniform (Luo and Al-Dahhan, 2008). The highest velocities occur near the sparger in proximity to the draft tube wall, while the local liquid velocity in the reactor center is significantly lower. This behavior can be linked to direct momentum input from the gas phase in the vicinity of the ring sparger outlets, where locally high gas holdup and intense bubble-induced mixing enhance liquid entrainment (Mudde, 2005). With increasing superficial gas velocity, a vortex structure forms in the riser, leading to a local counter flow. As a result, the short-time-averaged liquid velocity in the riser cross-section can decrease despite higher gas flow rates, since part of the liquid moves in the opposite direction within the recirculation zone. The observed fluctuations and spatially non-uniform velocity profiles are consistent with the inherently unsteady nature of gas–liquid flow in air-lift systems. In particular, the ring sparger induces a non-uniform gas release pattern, resulting in intermittent bubble swarms and strongly fluctuating local gas holdup. These intermittent gas structures lead to locally fluctuating momentum transfer to the liquid phase, reinforcing the observed velocity heterogeneity (Mudde, 2005). The vortex structure observed at higher surface gas velocities represents a short-term average of this highly time-dependent multiphase flow field, calculated using a five-second averaging window. It captures the prevailing flow structures whilst preserving the temporal variability inherent in the system.

3.5. Projection of potential three-phase operating regimes and derivation of a preliminary operating window

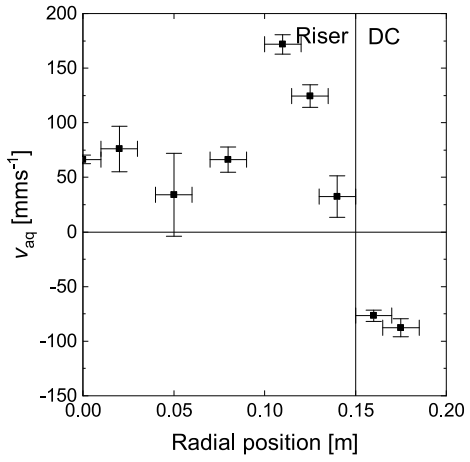
Three-phase operation requires that organic droplets introduced into the downcomer are not entrained into the riser by the circulating aqueous phase. A necessary criterion for entrainment is assumed to be when the downward liquid velocity exceeds the terminal rise velocity of the droplets, indicating the onset of solvent flooding. To assess this constraint, a theoretical estimate based on the measured two-phase hydrodynamic data was performed using 2-undecanone (density ρ_o =



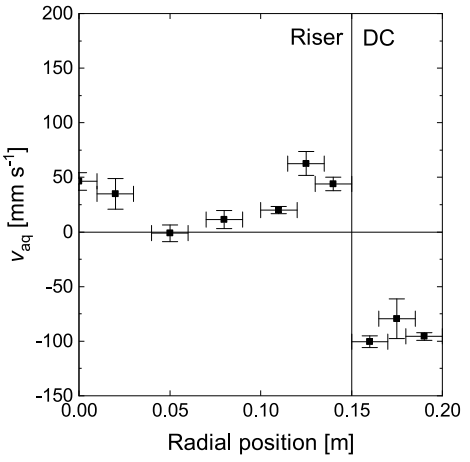
(a) Detection of the aqueous velocities inside the MPLR via PTV across the reactor cross-section at 0.001 m s^{-1}.



(b) Detection of the aqueous velocities inside the MPLR via PTV across the reactor cross-section at 0.01 m s^{-1}.



(c) Detection of the aqueous velocities inside the MPLR via PTV across the reactor cross-section at 0.02 m s^{-1}.



(d) Detection of the aqueous velocities inside the MPLR via PTV across the reactor cross-section at 0.044 m s^{-1}.

Fig. 6. Detection of the aqueous velocities inside the MPLR via PTV across the reactor cross-section at different gas superficial velocities. The position at 0 m corresponds to the center of the reactor, while the position at 200 mm corresponds to the wall of the reactor.

820 kg m^{-3}) as a representative organic phase. This solvent was selected because stable three-phase operation has previously been demonstrated with this system at laboratory scale, both in dedicated studies and under fermentation conditions (Grütering et al., 2024).

Among the correlations available in the literature for estimating droplet terminal rise velocity, the Schiller–Naumann (SN) correlation was chosen. This correlation is widely used to estimate the drag coefficient of spherical particles and is frequently applied as a first approximation for small liquid droplets (Clift et al., 1978). Compared with alternative correlations, it tends to predict lower rise velocities (Deng et al., 2018; Guan et al., 2020). Its use therefore provides a conservative estimate of the flooding limit, as entrainment of the organic phase is predicted already at comparatively low droplet velocities. The terminal rise velocity of individual droplets, u_o, was estimated from a force balance between buoyancy, gravity, and drag forces (Clift et al., 1978):

$$\frac{\pi}{6} d_o^3 (\rho_c - \rho_o) g = \frac{1}{2} C_d \rho_c \left(\frac{\pi}{4} d_o^2 \right) u_o^2. \tag{13}$$

Solving for u_o yields

$$u_o = \sqrt{\frac{4}{3} \cdot \frac{g\, d_o (\rho_c - \rho_o)}{C_d \rho_c}}, \tag{14}$$

where the Reynolds number is defined as

$$Re = \frac{\rho_c u_o d_o}{\mu_c}, \tag{15}$$

and the drag coefficient was calculated using the Schiller–Naumann correlation (Clift et al., 1978):

$$C_d = \frac{24}{Re} \left(1 + 0.15\, Re^{0.687} \right). \tag{16}$$

The Eqs. (14)–(16) were solved iteratively. Since the underlying model is based on a force balance on individual droplets in a stagnant continuous phase, it represents a simplified description of droplet hydrodynamics. To evaluate its applicability to the present system, additional three-phase experiments with 2-undecanone were conducted in the MPLR. For this purpose, the rise velocities of individual droplets in

the quiescent aqueous phase were determined experimentally and compared with the calculated values. The results are shown in Fig. 7. The organic droplets exhibited equivalent diameters between 1.2 and 3.1 mm. The measured rise velocity increased approximately linearly with droplet diameter, and this trend was captured qualitatively by the model. At the same time, the measured velocities were consistently above the predicted values, with the calculated curve closely describing the lower bound of the experimental scatter. The experimentally determined rise velocities ranged from approximately $78 \pm 18\,\mathrm{mm\,s^{-1}}$ to $132 \pm 11\,\mathrm{mm\,s^{-1}}$, whereas the model predicted velocities between 46 and $107\,\mathrm{mm\,s^{-1}}$ for the same droplet size range. The Schiller–Naumann correlation thus yields a conservative estimate of droplet rise velocity in the present system and was deemed suitable for further analysis. To estimate droplet motion in the aerated reactor, the quiescent rise velocity of the organic droplets was combined with the previously determined liquid velocity in the downcomer. The relative droplet velocity u_{rel} in the multiphase loop reactor at a given superficial gas velocity was calculated as

$$u_{rel} = u_o - |u_{aq,DC}|. \tag{17}$$

Here, u_o is the rise velocity of an organic droplet under quiescent conditions, while $u_{aq,DC}$ denotes the experimentally determined downward velocity of the aqueous phase in the downcomer. Accordingly, positive values of u_{rel} indicate upward droplet motion relative to the reactor, whereas negative values indicate downward transport and thus potential entrainment into the riser. The quiescent rise velocity u_o was taken either from the terminal rise velocities predicted by the Schiller–Naumann correlation $u_{o,SN}$, or from the experimentally determined mean values $u_{o,exp}$. To test this assumption, additional measurements were performed at superficial gas velocities of $0.001\,\mathrm{m\,s^{-1}}$ and $0.01\,\mathrm{m\,s^{-1}}$. The results are shown in Figs. 8(a), 8(b). At $0.001\,\mathrm{m\,s^{-1}}$, the relative droplet velocities $u_{rel,SN}$ obtained by directly combining the calculated quiescent droplet rise velocity with the measured aqueous-phase velocity significantly underestimate the experimentally determined values. Better agreement is obtained when u_{rel} is calculated using the experimentally measured rise velocity $u_{o,exp}$ under non-aerated conditions instead of the model-predicted quiescent rise velocity. In the investigated diameter range from approximately 1.2 mm to 2.2 mm, all measured droplets still exhibited upward motion. Even droplets with diameters of about 1.2 mm showed upward velocities close to $50\,\mathrm{mm\,s^{-1}}$, increasing to approximately $80\,\mathrm{mm\,s^{-1}}$ at around 2.0 mm. According to the Schiller–Naumann-based estimate, by contrast, droplets in the lower part of this size range would be expected to exhibit $u_{rel} \approx 0$ or only marginal upward motion. The experimental data therefore indicate that, at this low aeration rate, upward droplet transport occurs already at smaller droplet diameters than predicted by the model, whereas the approach based on the experimentally measured non-aerated rise velocity provides a closer description of the observed behavior.

At the higher superficial gas velocity of $0.01\,\mathrm{m\,s^{-1}}$, however, the trend changes. Compared with the weakly aerated case, the experimentally determined droplet velocities are lower over the entire measured size range, indicating reduced net upward transport of the organic droplets. The measured droplets covered a diameter range from approximately 1.3 mm to 1.9 mm. For droplets up to about 1.6 mm, the measured relative velocities remained close to $u_{rel} \approx 0$, indicating only marginal net upward motion. Clear upward transport was only observed for larger droplets, starting at approximately 1.7 mm, with measured relative velocities of about $15\,\mathrm{mm\,s^{-1}}$ and increasing to approximately $25\,\mathrm{mm\,s^{-1}}$. The Schiller–Naumann correlation, in contrast, predicts $u_{rel} \approx 0$ only at a droplet diameter of about 1.9 mm. The model therefore captures the overall order of magnitude, but still underestimates the experimentally observed upward transport. In contrast, the approach based on the experimentally measured rise velocity under non-aerated conditions $u_{rel,exp}$, corrected by the measured liquid

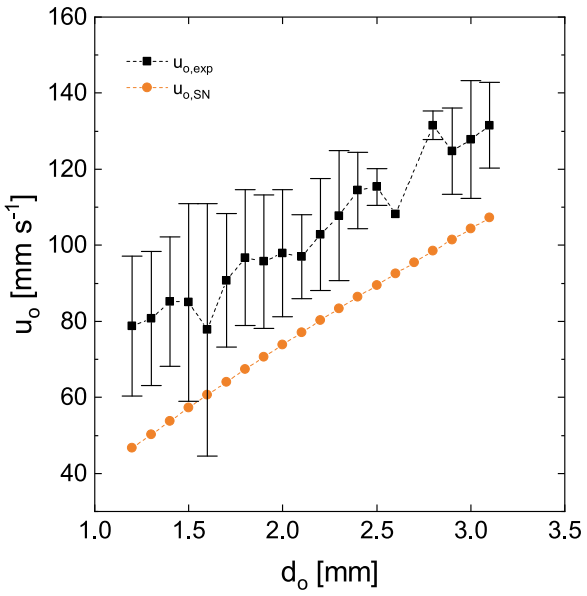
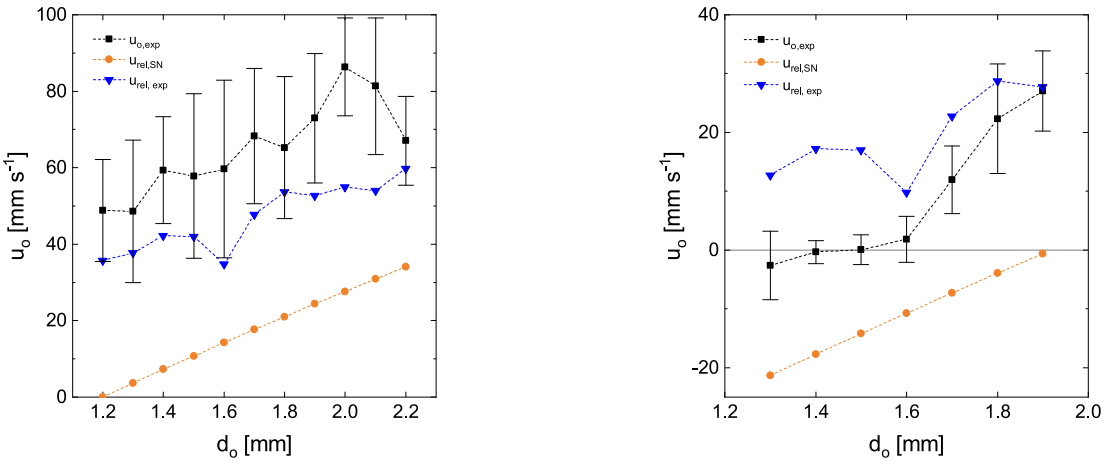


Fig. 7. Comparison of experimentally measured and model-predicted droplet rise velocities for individual 2-undecanone droplets of different diameters in the quiescent aqueous phase.

velocity in the aerated reactor, systematically overestimates the experimentally determined droplet velocities at a superficial gas velocity of $0.01\,\mathrm{m\,s^{-1}}$. This approach is therefore not suitable for a conservative estimate of droplet transport at higher superficial gas velocities, as it does not provide a robust lower bound for the experimental data. The Schiller–Naumann correlation therefore appears more appropriate for conservative assessment of the present system. As it predicts the lower bound of the measured rise velocities, it is likely to overestimate the minimum droplet diameter required for reliable upward transport. In a design context, this conservatism provides an inherent safety margin, but it may also lead to the selection of larger droplet diameters than are actually necessary, potentially at the expense of extraction performance.

For higher gas superficial velocities above $0.01\,\mathrm{m\,s^{-1}}$, no reliable droplet velocities could be determined because vortex formation in the aqueous phase within the riser disturbed the measurement conditions. In addition, the organic phase entered the riser from the upper reactor section, resulting in pronounced phase mixing. This caused substantial visual obscuration in the measurement region and prevented reliable detection of individual droplets in the downcomer by image analysis. Extending the accessible operating range of the MPLR would therefore require structural or process-related modifications. One possible approach is to optimize the gas sparging strategy in order to suppress vortex formation. Alternatively, the upper reactor section could be redesigned to prevent the organic phase from entering the riser. Both measures would aim to re-establish phase separation within the reactor while preserving the liquid circulation loop.

To translate the hydrodynamic constraints into a directly applicable design parameter, they were combined with the experimentally determined mass transfer and mixing characteristics. The relative velocity criterion was reformulated in terms of a minimum critical droplet diameter $d_{o,SN}$, defined as the smallest droplet size required to overcome the downward liquid flow and thus maintain counter-current operation. To ensure a conservative assessment, droplet rise velocities were estimated using the Schiller–Naumann correlation. The resulting synthesis is presented in Fig. 9, where the key performance indicators k_La, t_{mixing}, and the flooding criterion are jointly evaluated as a function of the superficial gas velocity u_g. The feasible operating region is defined by the intersection of the following criteria: (i) $k_La > 100\,\mathrm{h^{-1}}$,



(a) Droplet velocity as a function of droplet diameter at a superficial gas velocity of $0.001\,\mathrm{m\,s^{-1}}$.

(b) Droplet velocity as a function of droplet diameter at a superficial gas velocity of $0.01\,\mathrm{m\,s^{-1}}$.

Fig. 8. Comparison of measured droplet velocities in the MPLR with theoretically predicted relative droplet velocities.

(ii) $t_{\mathrm{mixing}} < 30\,\mathrm{s}$, and (iii) $u_{\mathrm{rel,SN}} > 0\,\mathrm{mm\,s^{-1}}$, ensuring that droplet rise overcomes downward liquid flow and prevents flooding. In addition to hydrodynamic stability, droplet size influences interfacial area and thus mass transfer and extraction performance. Based on literature reports on liquid–liquid extraction systems operating in dispersed-flow regimes, a droplet diameter of 2.5 mm is adopted here as a conservative upper bound, above which reduced interfacial area may impair extraction performance (Kumar and Hartland, 1996; Yu et al., 2023). Based on these constraints, four operating regimes are identified in Fig. 9: (I) insufficient mixing and mass transfer, (II) well mixed but mass-transfer limited, (III) well mixed with sufficient mass transfer and model-predicted fluid dynamic feasibility for counter-current droplet transport (candidate operating regime for future three-phase validation), and (IV) fluid dynamically feasible but characterized by large droplets, resulting in reduced extraction efficiency. This representation consolidates the governing process limitations and highlights the range of superficial gas velocities predicted to satisfy all imposed design criteria simultaneously. The presence of an organic phase may influence hydrodynamics, mass transfer, and mixing due to changes in fluid properties and interfacial effects. These interactions are not captured in the present two-phase model and may become relevant for other solvent systems or higher dispersed-phase fractions. The operating window should therefore be interpreted as a first-order engineering design tool based on two-phase data, and experimental validation under three-phase conditions remains necessary.

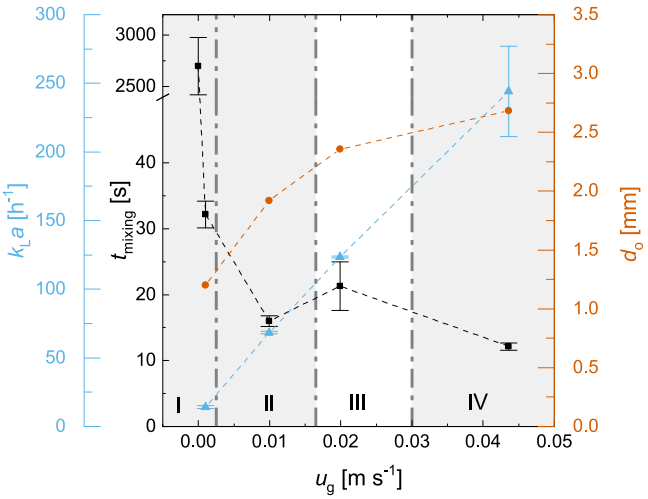


Fig. 9. Design-oriented operating window of the multiphase loop reactor as a function of superficial gas velocity u_g based on gas–liquid data. Thresholds for mass transfer, mixing, and hydrodynamic stability define the feasible operating region.

4. Conclusion

This study presents a pilot-scale setup for investigating the key fluid dynamic characteristics of a multiphase loop reactor. Robust measurement methods were established to qualify design- and operation-relevant parameters, including gas holdup, volumetric mass transfer coefficient, mixing time and liquid circulation velocity. The applied methods enabled reproducible characterization of the reactor under scale-relevant conditions. The reactor was investigated at superficial gas velocities ranging from 0.001 to $0.044\,\mathrm{m\,s^{-1}}$. Steady state was reached within 15 s, as indicated by stable gas holdup values. Gas holdup increased with superficial gas velocity, with a change in slope between 0.001 and $0.01\,\mathrm{m\,s^{-1}}$ suggesting a transition in flow regime. The volumetric mass transfer coefficient increased continuously with superficial gas velocity, exceeding $100\,\mathrm{h^{-1}}$ between 0.01 and $0.02\,\mathrm{m\,s^{-1}}$. Mixing times decreased significantly with the onset of convective transport and reached a plateau at gas velocities above $0.01\,\mathrm{m\,s^{-1}}$, indicating efficient bulk mixing under these conditions. The liquid flow field was characterized through liquid velocity distributions across the reactor cross-section. The expected circulation between downcomer and riser was confirmed. While the downcomer exhibits comparatively uniform flow behavior, the riser shows pronounced spatial non-uniformities, reflecting more complex hydrodynamic conditions.

To assess the feasibility of three-phase operation, the measured two-phase hydrodynamics were combined with a droplet rise velocity model. For this purpose, the Schiller–Naumann correlation was used as a conservative estimate of the lower bound of droplet rise velocity. Additional three-phase experiments with 2-undecanone showed that this approach provides a suitable conservative basis for assessing droplet transport. At least up to a superficial gas velocity of $0.01\,\mathrm{m\,s^{-1}}$, however, the model remained clearly conservative, as upward droplet transport was experimentally observed already for smaller droplets than predicted by the model threshold. This indicates that smaller droplets may be used in practice without being entrained by the downward aqueous flow. At higher superficial gas velocities, experimental validation was no longer possible because vortex formation in the riser drew organic

phase from the upper reactor section into the riser, causing severe visual obscuration and preventing reliable optical droplet tracking. Based on these results, a critical droplet diameter was derived by relating the downward aqueous-phase velocity in the downcomer to droplet rise behavior. This criterion provides a first estimate of whether counter-current operation can be maintained for a given solvent system and droplet size, although it does not capture phase interactions present in real three-phase systems.

To integrate these findings, the hydrodynamic constraints were combined with mass transfer and mixing characteristics in a design-oriented operating window. This representation relates the key performance indicators $k_L a$, t_{mixing}, and the critical droplet diameter $d_{o,SN}$ to the superficial gas velocity, thereby identifying a range of operating conditions that simultaneously satisfy all relevant criteria. The resulting operating window suggests that medium to high superficial gas velocities are the most promising candidates for stable and efficient operation, as these conditions are predicted to provide sufficient oxygen transfer and rapid mixing while maintaining model-predicted feasibility for counter-current extraction. The presented operating window should be understood as a first-order engineering estimate based on two-phase data and simplified droplet transport, with partial validation in three-phase experiments for the low-aeration range. Accordingly, it should be interpreted as a model-based design framework rather than an experimentally validated three-phase operating envelope. Effects arising from the presence of an organic phase, such as changes in fluid properties, interfacial phenomena, and dispersed-phase interactions, are not captured in the current framework. Therefore, experimental validation under three-phase conditions is required to confirm the predicted behavior. Overall, the developed methodology and pilot-scale platform provide a structured basis for analyzing and designing the multiphase loop reactor and support future studies aimed at validating and extending the operating window for different reactor configurations, process conditions, solvent systems, and bioprocesses.

Abbreviations

aq	aquous
c	continuous phase
crit	critical
cor	correction
d	drag
DC	Downcomer
eff	effective
exp	experimental
g	gas
o	organic
p	particle
rel	relative
SN	Schiller–Naumann

CRediT authorship contribution statement

Diana Wall: Writing – review & editing, Writing – original draft, Visualization, Validation, Supervision, Software, Project administration, Methodology, Investigation, Formal analysis, Data curation, Conceptualization. **Maurice Bastard:** Writing – original draft, Visualization, Software, Investigation. **Andreas Jupke:** Resources, Funding acquisition, Conceptualization.

Declaration of competing interest

The authors declare that they have no known competing financial interests or personal relationships that could have appeared to influence the work reported in this paper.

Acknowledgments

This research was done within the BioSC project MK ScaLoop. The scientific activities of the Bioeconomy Science Center were financially supported by the Ministry of Culture and Science within the framework of the NRW Strategieprojekt BioSC (No. 005-2012-0107).

Appendix A. Supplementary data

Supplementary material related to this article can be found online at https://doi.org/10.1016/j.cherd.2026.06.054.

References

Adedeji Olalekan Iwogbemi, Ambrose Sunny Okorie, 2025. Biotechnological pathways for transitioning oil refineries to bio-based refineries. Int. J. Pet. Gas Eng. Res. (8), 13–24. http://dx.doi.org/10.37745/ijpger.17.

Alicke, Alexandra, Jaensson, Nick O., Vermant, Jan, 2025. Mechanistic insights into emulsion destabilization by electric fields. Langmuir : ACS J. Surf. Colloids 41 (39), 26589–26604. http://dx.doi.org/10.1021/acs.langmuir.5c02307.

Bai, W., 2010. Experimental and Numerical Investigation of Bubble Column Reactors (Phd Thesis). Technische Universiteit Eindhoven, http://dx.doi.org/10.6100/IR693280.

Bednarz, A., Weber, B., Schmidt, M., 2017. Mehrphasenschlaufenreaktor. Eur. Pat. Bull. 36 (WO2017149099).

Brennen, Christopher E., 2005. Fundamentals of Multiphase Flow. Cambridge university press, ISBN: 978-0521848046.

von Campenhausen, Maximilian, et al., 2023. Novel multiphase loop reactor with improved aeration prevents excessive foaming in rhamnolipid production by Pseudomonas putida. Discov. Chem. Eng. 3 (1), 1–14. http://dx.doi.org/10.1007/s43938-023-00018-5.

Chaichol, Patchara, Weeranoppanant, Nopphon, 2023. Advances in in situ and in-line liquid–liquid extraction for bioprocess intensification. React. Chem. Eng. 8 (10), 2387–2402. http://dx.doi.org/10.1039/D3RE00266G.

Christi, M.Y., Moo-Young, M., 1987. AIrlift reactors: characteristics, applications and design considerations. Chem. Eng. Commun. 60 (1–6), 195–242. http://dx.doi.org/10.1080/00986448708912017.

Clift, Roland, Grace, John R., Weber, Martin E., 1978. Bubbles, Drops, and Particles. Academic Press, ISBN: 978-0121769505.

De Brabander, Pieter, et al., 2021. In situ product recovery of bio-based industrial platform chemicals: A guideline to solvent selection. Fermentation 7 (1), 26. http://dx.doi.org/10.3390/fermentation7010026.

Demling, Philipp, et al., 2021. Pseudomonas putida KT2440 endures temporary oxygen limitations. Biotechnol. Bioeng. 118 (12), 4735–4750. http://dx.doi.org/10.1002/bit.27938.

Deng, Chaojun, et al., 2018. Preparation of micron-sized droplets and their hydrodynamic behavior in quiescent water. Braz. J. Chem. Eng. 35, 709–720. http://dx.doi.org/10.1590/0104-6632.20180352s20160659.

Dianingsih, Nurlita, Purnomo, Eko Hari, Muchtadi, Tien R., 2016. Sifat reologi dan stabilitas fisik minuman emulsi minyak sawit. J. Teknol. Ind. Pangan 27 (2), 165–174. http://dx.doi.org/10.6066/jtip.2016.27.2.165.

Doran, Pauline M., 1995. Bioprocess engineering principles. ISBN: 978-0-12-220855-3.

Escobar, S, et al., 2016. Influence of oxygen transfer on pseudomonas putida effects on growth rate and biodesulfurization capacity. Bioprocess Biosyst. Eng. 39 (4), 545–554. http://dx.doi.org/10.1007/s00449-016-1536-6.

Fontenot, Kevin, Schork, F. Joseph, 1993. Sensitivities of droplet size and stability in monomeric emulsions. Ind. Eng. Chem. Res. 32 (2), 373–385. http://dx.doi.org/10.1021/ie00014a014.

Garcia-Ochoa, Felix, Gomez, Emilio, 2009. Bioreactor scale-up and oxygen transfer rate in microbial processes: an overview. Biotech. Adv. 27 (2), 153–176. http://dx.doi.org/10.1016/j.biotechadv.2008.10.006.

Grütering, Carolin, et al., 2024. Methyl ketones: a comprehensive study of a novel biofuel. Sustain. Energy Fuels 8 (9), 2059–2072. http://dx.doi.org/10.1039/D4SE00035H.

Guan, Xiaoping, et al., 2020. CFD simulation of gas-liquid flow in stirred tanks: Effect of drag models. Chem. Eng. J. 386, 121554. http://dx.doi.org/10.1016/j.cej.2019.04.134.

Hwang, Shyh-Jye, Cheng, Yi-Lung, 1997. Gas holdup and liquid velocity in three-phase internal-loop airlift reactors. Chem. Eng. Sci. 52 (21–22), 3949–3960. http://dx.doi.org/10.1016/S0009-2509(97)88931-2.

Kalaga, Dinesh V, et al., 2017. Investigation of hydrodynamics in bubble column with internals using radioactive particle tracking (RPT). AIChE J. 63 (11), 4881–4894. http://dx.doi.org/10.1002/aic.15829.

Kennedy, Gregory J., et al., 2024. Biomass demineralization and pretreatment strategies to reduce inhibitor concentrations in itaconic acid fermentation by aspergillus terreus. Biomass 4 (4), 1122–1141. http://dx.doi.org/10.3390/biomass4040062.

Kumar, Arun, Hartland, Stanley, 1996. Unified correlations for the prediction of drop size in liquid- liquid extraction columns. Ind. Eng. Chem. Res. 35 (8), 2682–2695. http://dx.doi.org/10.1021/ie950674w.

Lee, Kyungsoo, et al., 2019. Enhanced production of styrene by engineered escherichia coli and in situ product recovery (ISPR) with an organic solvent. Microb. Cell Factories 18 (1), 79. http://dx.doi.org/10.1186/s12934-019-1129-6.

Li, Lifeng, et al., 2022. Hydrodynamics and mass transfer of concentric-tube internal loop airlift reactors: A review. Bioresour. Technol. 359, 127451. http://dx.doi.org/10.1016/j.biortech.2022.127451.

Luo, Hu-Ping, Al-Dahhan, Muthanna H., 2008. Local characteristics of hydrodynamics in draft tube airlift bioreactor. Chem. Eng. Sci. 63 (11), 3057–3068. http://dx.doi.org/10.1016/j.ces.2008.03.015.

Luo, Hu-Ping, Al-Dahhan, Muthanna H., 2010. Local gas holdup in a draft tube airlift bioreactor. Chem. Eng. Sci. 65 (15), 4503–4510. http://dx.doi.org/10.1016/j.ces.2010.04.037.

Maiorella, Brian, Blanch, Harvey W., Wilke, Charles R., 1983. By-product inhibition effects on ethanolic fermentation by saccharomyces cerevisiae. Biotechnol. Bioeng. 25 (1), 103–121. http://dx.doi.org/10.1002/bit.260250109.

Maxey, Martin R., Riley, James J., 1983. Equation of motion for a small rigid sphere in a nonuniform flow. Phys. Fluids 26 (4), 883–889. http://dx.doi.org/10.1063/1.864230.

Mudde, Robert F., 2005. Gravity-driven bubbly flows. Annu. Rev. Fluid Mech. 37 (1), 393–423. http://dx.doi.org/10.1146/annurev.fluid.37.061903.175803.

Park, Chang-Ho, Geng, Qinghuang, 1992. Simultaneous fermentation and separation in the ethanol and ABE fermentation. Sep. Purif. Methods 21 (2), 127–174. http://dx.doi.org/10.1080/03602549208021421.

Rosso, Diego, Stenstrom, Michael K, Garrido-Baserba, Manel, et al., 2023. Aeration and mixing. In: Chen, G., Ekama, G.A., van Loosdrecht, M.C.M., Brdjanovic, D. (Eds.), Biological Wastewater Treatment: Principles, Modeling and Design, second ed. http://dx.doi.org/10.2166/9781789062304_0317.

Salas-Villalobos, Ulises A, et al., 2021. In situ product recovery as a strategy for bioprocess integration and depletion of inhibitory products. J. Chem. Technol. Biotechnol. 96 (10), 2735–2743. http://dx.doi.org/10.1002/jctb.6797.

Schiller, Ludwig, Naumann, Z., 1933. Über die grundlegenden berechnungen bei der Schwerkraftaufbereitung. Z. Vereins Dtsch. Ingenieure 77 (12), 318–320.

Smith, Kathryn H., Bowser, Tim, Stevens, Geoffrey W., 2008. Performance and scale-up of karr reciprocating plate extraction columns. Ind. Eng. Chem. Res. 47 (21), 8368–8375. http://dx.doi.org/10.1021/ie800581u.

Weilnhammer, Christian, Blass, Eckhart, 1994. Continuous fermentation with product recovery by in-situ extraction. Chem. Eng. Technol.: Ind. Chem.-Plant Equip.-Process Eng.-Biotechnol. 17 (6), 365–373. http://dx.doi.org/10.1002/ceat.270170602.

Wilkinson, Peter M., Spek, Arie P., van Dierendonck, Laurent L., 1992. Design parameters estimation for scale-up of high-pressure bubble columns. AIChE J. 38 (4), 544–554. http://dx.doi.org/10.1002/aic.690380408.

Xue, Chuang, et al., 2015. Evaluation of hydrophobic micro-zeolite-mixed matrix membrane and integrated with acetone–butanol–ethanol fermentation for enhanced butanol production. Biotechnol. Biofuels 8 (1), 105. http://dx.doi.org/10.1186/s13068-015-0288-x.

Yu, Sicen, et al., 2023. Mass transfer and droplet behaviors in liquid-liquid extraction process based on multi-scale perspective: a review. Separations 10 (4), 264. http://dx.doi.org/10.3390/separations10040264.

Yusuf, Jamiu Adeniyi, Ojedokun, R.O., 2024. The role of bio-based innovations in circular economy: A biochemical and economic perspective. J. Med. Sci. Biol. Chem. 1 (1), 21–27. http://dx.doi.org/10.69739/jmsbc.v1i1.148.

Zaidi, Ali Abbas, 2020. Settling characteristics of bidisperse dilute suspension in the vortex shedding regime. Phys. Fluids 32 (9), http://dx.doi.org/10.1063/5.0011538.

Zhang, Qi, et al., 2015. Substrate and product inhibition on yeast performance in ethanol fermentation. Energy Fuels (ISSN: 0887-0624) 29 (2), 1019–1027. http://dx.doi.org/10.1021/ef502349v.

Zhong, Fan, et al., 2022. Flow regimes characteristics of industrial-scale center-rising airlift reactor. Chem. Eng. J. 430, 133067. http://dx.doi.org/10.1016/j.cej.2021.133067.